JACS
JOURNAL OF THE AMERICAN CHEMICAL SOCIETY
pubs.acs.org/JACS
Article

Selectivity in Yttrium Manganese Oxide Synthesis via Local Chemical Potentials in Hyperdimensional Phase Space

Paul K. Todd,[\$] Matthew J. McDermott,[\$] Christopher L. Rom, Adam A. Corrao, Jonathan J. Denney, Shyam S. Dwaraknath, Peter G. Khalifah, Kristin A. Persson, and James R. Neilson*

Cite This: https://doi.org/10.1021/jacs.1c06229
Read Online

ACCESS | Metrics & More | Article Recommendations | Supporting Information

ABSTRACT: In sharp contrast to molecular synthesis, materials synthesis is generally presumed to lack selectivity. The few known methods of designing selectivity in solid-state reactions have limited scope, such as topotactic reactions or strain stabilization. This contribution describes a general approach for searching large chemical spaces to identify selective reactions. This novel approach explains the ability of a nominally "innocent" Na_2CO_3 precursor to enable the metathesis synthesis of single-phase $Y_2Mn_2O_7$: an outcome that was previously only accomplished at extreme pressures and which cannot be achieved with closely related precursors of Li_2CO_3 and K_2CO_3 under identical conditions. By calculating the required change in chemical potential across all possible reactant-product interfaces in an expanded chemical space including Y, Mn, O, alkali metals, and halogens, using thermodynamic parameters obtained from density functional theory calculations, we identify reactions that minimize the thermodynamic competition from intermediates. In this manner, only the Na-based intermediates minimize the distance in the hyperdimensional chemical potential space to $Y_2Mn_2O_7$, thus providing selective access to a phase which was previously thought to be metastable. Experimental evidence validating this mechanism for pathway-dependent selectivity is provided by intermediates identified from *in situ* synchrotron-based crystallographic analysis. This approach of calculating chemical potential distances in hyperdimensional compositional spaces provides a general method for designing selective solid-state syntheses that will be useful for gaining access to metastable phases and for identifying reaction pathways that can reduce the synthesis temperature, and cost, of technological materials.

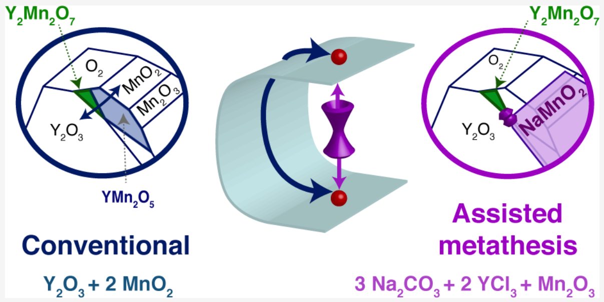

■ INTRODUCTION

Molecular reactions use catalysts to increase the rate of reaction and achieve selectivity by modifying specific barriers in the reaction pathway. However, this approach cannot be readily translated to the synthesis of nonmolecular compounds, which are found in a wide range of industrial applications ranging from batteries in electronic devices to cement in concrete. To achieve selective control over solid-state reactions, a necessary first step is "turning down the heat" enough to prevent nonselective phase interconversion.[1] An extreme example of this strategy is a topotactic reaction involving ion exchange in which only a single type of atom is mobile (e.g., cations[2] or anions[3,4]), which has enabled lithium-ion battery technology.[5] However, such reactions require a relatively inert framework that facilitates the mobility of these ions. Another route to selective synthesis is epitaxial strain stabilization on a single-crystal or polycrystalline substrate.[6] While algorithms to search for suitable substrates exist,[7] the epitaxial stabilization requires the synthesis of a chemically compatible lattice-matched substrate, which yields only a limited amount of material that is necessarily attached to the underlying substrate.

To address the challenge of designing selective reactions in solid-state chemistry, one must have an understanding of how the reaction proceeds. Pairwise reactions at interfaces between solids dominate selection of a reaction pathway.[8,9] With the inclusion of additional elements, as in metathesis reactions,[10,11] one can avoid highly stable and thus unreactive intermediates, as demonstrated in the formation of $MgCr_2S_4$ while avoiding the inert reactant Cr_2S_3.[12,13] In the preparation of complex oxides, "assisted" metathesis reactions reach quantitative yields at lower temperatures than conventional ceramic reactions,[14] and they can even exhibit product selectivity depending on which alkali (A = Li, Na, K) carbonate precursor is used. This is seen for the reactions of $3\ A_2CO_3 + 2\ YCl_3 + Mn_2O_3$, where in the case of Li_2CO_3, the reaction selectively forms

Received: June 16, 2021

orthorhombic $YMnO_3$, Na_2CO_3 yields $Y_2Mn_2O_7$, and K_2CO_3 does not yield selectivity.[15]

A central challenge of this contribution is to understand the origin of the different product outcomes that result from changing an ancillary precursor that is not directly involved in any elementary reaction producing a yttrium manganese oxide. In conventional stoichiometric reactions using binary yttrium oxide and manganese oxide precursors, hexagonal $YMnO_3$, denoted h-$YMnO_3$, forms at temperatures greater than 950 °C.[16,17] Previous reports have described the synthesis of $Y_2Mn_2O_7$ under high temperatures and highly oxidizing conditions (1100 °C and 4 GPa with $KIO_4 \rightarrow KIO_3 + 1/2O_2$)[18] or hydrothermally under oxidizing conditions (NaOH, $NaClO_3$ in H_2O at 500 °C and 3 GPa),[19] leading to its previous characterization as a metastable phase.[20] Interestingly, thermogravimetric analysis shows the $Y_2Mn_2O_7$ pyrochlore to be stable up to 800 °C, above which it decomposes to the perovskite $YMnO_3$.[19] Therefore, if $Y_2Mn_2O_7$ is stable at the lower temperatures, its stability cannot solely explain why only the sodium-based assisted metathesis precursors are selective for its formation given the low reaction temperatures for all of the alkali metathesis reactions.

Here, using temperature-dependent synchrotron powder X-ray diffraction (SPXRD) experiments to study the $Y_2Mn_2O_7$-forming assisted metathesis reaction with a sodium precursor, $Mn_2O_3 + 2\ YCl_3 + 3\ Na_2CO_3 + 1/2\ O_2 \rightarrow Y_2Mn_2O_7 + 6\ NaCl + 3\ CO_2$, we identify a specific reaction pathway dependent on the formation of Y_2O_3 and its reaction with Na_xMnO_2 intermediates. Density functional theory (DFT) derived thermochemistry reveals that $Y_2Mn_2O_7$ is thermodynamically stable below $T \approx 1100$ °C and that sodium-based intermediates provide selective formation of this phase by circumventing the formation of other Y−Mn−O intermediates (e.g., $YMnO_3$ and YMn_2O_5). This sodium based reaction differs from the equivalent reactions with Li_2CO_3 and K_2CO_3, which we previously showed instead yield $YMnO_3$, with a reaction temperature as low as 500 °C.[21,22] We attribute the selective formation of $Y_2Mn_2O_7$ to the distance of the Na-based intermediates in chemical potential space, which is shown visually on the chemical potential diagram and is numerically calculated between the stability regions of the reactants and products in a reaction. These methods, applied to easily retrievable materials data, now allow one to search for selective reactions over large, hyperdimensional compositional spaces.

■ METHODS

Experimental Methods. All reagents were prepared, stored, and weighed in an argon-filled glovebox with O_2 and H_2O levels ≤0.1 ppm. Manganese(III) oxide (Sigma-Aldrich 99%) was purified by heating Mn_2O_3 in an alumina boat at 1 °C/min to 700 °C for 16 h in air and quenched into the glovebox; purity was verified by powder X-ray diffraction (PXRD). Manganese(IV) oxide (Sigma-Aldrich ≥99%), YCl_3 (Alfa Aesar 99.9%), sodium carbonate (ACROS Organics 99.5%), and manganese(II) carbonate (Sigma-Aldrich ≥99.99%) were purchased and stored under argon. All gases (O_2, Ar, He) were purchased through Airgas at the Ultra High Purity grade (99.999%). $NaMnO_2$ (*C*2/*m*) was prepared by mixing manganese(III) oxide and sodium carbonate in a 1:1 molar ratio, grinding for 15 min in an agate mortar and pestle, and pelleting using a 1/4 in die under ∼1 tn of force. The pellet was placed upon a sacrificial layer of powder in an alumina crucible and heated in a muffle furnace at 1 °C/min to 700 °C for 10 h. The reaction was subsequently quenched into the antechamber of the glovebox and stored under argon. Similarly, $Na_{0.7}MnO_2$ (*Cmcm*) was prepared by mixing manganese(II) carbonate and sodium carbonate in a 0.70:1 Na:Mn ratio following the same pellet preparation as $NaMnO_2$. The reaction was performed by heating at 5 °C/min to 1050 °C for 15 h and then quenched into the antechamber of a glovebox and stored in an argon atmosphere. Y_2O_3 was purified of hydroxide in an alumina boat at 1 °C/min to 900 °C for 4 h in air, cooled to 200 °C at 1 °C/min for 12 h, and quenched into the glovebox. YOCl was prepared by heating $YCl_3\cdot 6H_2O$ in an alumina boat to 350 °C at 10 °C/min for 4 h in air. The YOCl product formed as the *P*4/*nmn* PbClF structure-type. All prepared reactants were confirmed using laboratory PXRD. Preparations for *ex situ* assisted metathesis reactions have been described in detail previously where reaction yields match the expected $Y_2Mn_2O_7$:6NaCl by PXRD (14.2(3) mol % $Y_2Mn_2O_7$).[15] Laboratory PXRD data were collected on a Bruker D8 Discover diffractometer using Cu Kα radiation and a Lynxeye XE-T position-sensitive detector.

For temperature-dependent *in situ* assisted metathesis reactions that produce carbon dioxide as a byproduct, open-ended quartz capillaries (1.1 mm OD) were packed in a glovebag under argon using glass wool as a plug. Synchrotron X-ray diffraction experiments were performed at beamline 17-BM-B (λ = 0.2415 Å) at the Advanced Photon Source (APS) at Argonne National Laboratory using a PerkinElmer plate detector at a distance of 700 mm. All capillaries were loaded into a flow-cell apparatus equipped with resistive heating elements and heated at 10 °C/min.[23] Gas flow (O_2, He) was controlled through mass flow controllers at a rate of 0.2 cc/min. Assisted-metathesis reactions were heated to a maximum temperature of 850 °C while the sample continuously rocked at ±5° around the axis of the capillary. Diffraction patterns were collected every two seconds and summed every 20 s for powder averaging. Plate detector images were integrated using GSAS-II and calibrated using a LaB_6 standard.

All Rietveld refinements were performed using TOPAS v6. Due to the number and positional overlap of intermediates during the sequential refinements, thermal displacement parameters were fixed at 5 Å^2, and the full-width-half-max using a Lorentzian polynomial was fixed at 178 nm to better account for changes in peak intensity during the reaction. In order to compare the relative fractions of phases determined from Rietveld calculations,[24] a weighted scale factor (WSF) is defined as $Q_p = S_p \cdot V_p \cdot M_p$ where Q_p = weighted scale factor of phase p, S_p = Scale factor calculated from Rietveld for phase p, V_p is the volume of the unit cell for phase p, and M_p is the atomic mass of the unit cell for phase p. It should be noted that we omit the Brindley coefficient for microabsorption correction in our calculation of weighted scale factor due to the unreliable refinement of particle sizes for individual phases. Amorphous material and product lost as vapor are not accounted for in the sequential refinement. We reference all phases by their nominal stoichiometric formula; however, the actual chemical formula may be distinct from the written formula as XRD data alone cannot typically resolve nonstoichiometric compounds.

It has been recently demonstrated by some of us that f^* diagrams are a powerful tool for understanding defects in chemical systems with three different crystallographic sites, allowing a diffraction analog of a ternary phase diagram to be calculated in which each axis represents the relative scattering power of each crystallographic site (at $2\theta = 0$) rather than the chemical composition.[25,26] The f^* diagram method is applied here with a slight modification to understand the evolution of defects within the Na_xMnO_2 intermediates. The *C*2/*m* P3 structure has three distinct crystallographic sites (one for each element), whereas the *Cmcm* Birnessite P2 phase has four distinct crystallographic sites (2 Na, 1 Mn, 1 O) rather than three. Therefore, the scattering powers of the two Na sites were summed together in the construction of the f^* diagram.

Computational Methods. *Calculating thermodynamic free energies.* DFT-based atomic structures and formation enthalpies for material phases in the Y−Mn−O−Na−Li−K chemical system were acquired from the Materials Project (MP) database, version V2021.05.13[27] Gibbs free energies of formation, $\Delta_f G^0(T)$, of solid DFT compounds were estimated using the machine-learned Gibbs free energy descriptor approach implemented by Bartel et al.[28] and applied to MP data. The pymatgen package was used to perform convex hull phase stability analysis.[29]

To model the energetics of reactions occurring in flowing O_2 gas, the grand potential energy, Φ, was used as the relevant thermodynamic potential

$$\Phi = G(P, T) - \mu_O N_O \tag{1}$$

where Φ is normalized to the number of nonoxygen atoms. Since in place of $G(P,T)$ we used standard Gibbs free energies of formation, $\Delta G_f^0(T = 650\ ^\circ C)$, the chemical potential of oxygen was assigned a value of zero, i.e., $\mu_O = \mu_O^0$ (p = 0.1 MPa, T = 650 °C). While this did not result in a shift in the total grand potential energy of any particular phase, it did change the number of atoms used for normalization and hence affected the magnitude of the normalized reaction energies, $\Delta\Phi_{rxn}$.

Construction of chemical potential diagrams. Chemical potential diagrams, as well as their more traditional two-dimensional versions (predominance diagrams), were constructed using the methodology described by Yokokawa.[30] We used an algorithmic approach inspired by a similar method for construction of Pourbaix diagrams,[31] which is briefly summarized here.

For a pure substance with N atoms per chemical formula unit, consisting of n unique elements indexed i with concentrations of x_i, its hyperplane in n-dimensional chemical space is defined via the equation

$$\sum_{i=1}^{n} x_i(\mu_i - \mu_i^0) = \frac{1}{N}\Delta G_f^0(T) \tag{2}$$

where the standard Gibbs free energy of formation, $\Delta G_f^0(T)$, has been normalized to an energy-per-atom basis by dividing by the total number of atoms per formula unit, N. Note that all reference chemical potentials μ_i^0 are set to zero when working with elements in their standard states.

Following the construction of hyperplanes for all phases in the chemical system, the stability domains are acquired by taking the convex hull of all points belonging to that phase in the set of intersections of the lowest energy hyperplanes, as calculated with the HalfspaceIntersection code implemented in SciPy.[32] In this construction, each stability region is a convex $n-1$-dimensional polytope in n-dimensional chemical potential space. Since many possible chemical reactions involve more than n = 3 elements, we must take additional steps to visualize the hyperdimensional (n > 3) phase boundaries relevant to the reactions in this work. This can be accomplished by (1) using clever transformations of the axes, (2) setting one or more chemical potentials to fixed values, or (3) taking a slice of the relevant chemical potential polytopes in lower dimensions. Here, we choose the third option, which uniquely allows for comparison across the full Y−Mn−O−Na−Li−K−Cl assisted metathesis system. Phases that do not directly appear on the generalized chemical potential diagram in three dimensions, e.g., $AMnO_2$ in the Y−Mn−O subspace, are thus computed first in higher dimension chemical potential space (A−Y−Mn−O) and then sliced to plot in lower-dimensional subspace. In the case of $AMnO_2$, these regions appear as three-dimensional polyhedra due to the added degree of freedom in the chemical potential of the alkali element, μ_A. These polyhedra also at least partially contact the stability areas of Y−Mn−O compounds, indicating where phases are adjacent in higher-dimensional space.

The "chemical potential distance", $\Delta\mu_{\min}(P_a, P_b)$, between any two phases P_a and P_b was calculated geometrically by finding the minimum Euclidean distance between the domains (i.e., the convex stability polytopes) of each phase on the chemical potential diagram. This was accomplished practically by computing the minimum Euclidean distance between all pairs of vertices ($\boldsymbol{\mu}_{a_i}$, $\boldsymbol{\mu}_{b_j}$) defining each of the two convex polytopes of phases P_a and P_b

$$\Delta\mu_{\min}(P_a, P_b) = \min_{i,j}\left\{\left\|\boldsymbol{\mu}_{a_i} - \boldsymbol{\mu}_{b_j}\right\|\right\} \tag{3}$$

While the minimum distance between vertices is not necessarily equivalent to the minimum distance between any facet of the polytopes, the implementation of the more accurate distance calculation is nontrivial. We thus found the vertex based k-d tree method, as implemented in SciPy, to be an appropriate trade-off between computational complexity and accuracy.

Enumerating reactions with $Y_2Mn_2O_7$ as a product. Chemical reactions with $Y_2Mn_2O_7$ as a product were enumerated via a network-based approach described in a previous work[33] and implemented in the reaction-network Python package.[34] To summarize, the enumeration approach is a combinatorial brute force approach whereby every combination of phases up to a size of n is considered both as a possible set of reactants or products. The set of all possible reactions is calculated by taking the Cartesian product between the set of reactant phase combinations and product phase combinations and filtering by whether it is possible to write a stoichiometrically balanced reaction equation between the reactants and products. In this work, reactions up to a size n = 2 are enumerated from the set of 2,878 phases predicted to be stable at T = 650 °C within the alkali metal (Li, Na, K, Rb, Cs), halogen (F, Cl, Br, I), carbon (C), and target (Y, Mn, O) chemical system. To account for the system being open to oxygen gas, we also consider reaction equations with oxygen as an optional reactant or product beyond the n = 2 limitation.

The enumerated reactions were compared against each other by using both the normalized reaction free energy and a "total" chemical potential distance for the reaction as "cost" variables. For the purposes of ranking reactions, the total cost of a reaction, C, was calculated using the softplus function with an equally weighted mean between the two cost variables

$$C = \ln\left(1 + \frac{273}{T}\exp\left(\frac{\Delta\Phi_{rxn} + \sum\Delta\mu_{\min}}{2}\right)\right) \tag{4}$$

where T corresponds to a temperature of T = 923 K, the reaction energy, $\Delta\Phi_{rxn}$, corresponds to the normalized change in grand potential energy, and $\sum\Delta\mu_{\min}$ represents the total chemical potential distance for a reaction, which is calculated as the sum of the (minimum) chemical potential distances between all possible pairwise interfaces in the reaction, excluding the interface(s) between the reactants. For example, in the hypothetical reaction A + B → C + D, the total chemical potential distance is calculated by taking the summation of $\Delta\mu_{\min}$(A, C), $\Delta\mu_{\min}$(A, D), $\Delta\mu_{\min}$(B, C), $\Delta\mu_{\min}$(B, D), and $\Delta\mu_{\min}$(C, D).

The full set of enumerated chemical reactions, as well as all experimental raw data, processed data, data processing scripts, and figure plotting scripts, are available at https://github.com/GENESIS-EFRC/y2mn2o7-selectivity. The entire reaction enumeration and ranking approach has also been implemented within the aforementioned reaction-network Python package[34] and can be applied in a similar fashion to recommend precursors for synthesizing other target materials. The applicability of this approach beyond the Y−Mn−O system is the subject of future work(s).

■ RESULTS AND DISCUSSION

Reaction Pathway from Phase Evolution. *In situ* synchrotron powder X-ray diffraction (SPXRD) studies were used to identify the intermediate phases and reaction pathways that permit the selective formation of $Y_2Mn_2O_7$ through assisted metathesis reactions with Na_2CO_3. Figure 1 shows the integrated SPXRD diffraction patterns collected during the reaction: $Mn_2O_3 + 2\ YCl_3 + 3\ Na_2CO_3$. Data were collected during heating to 650 °C at 10 °C/min then dwelling at 650 °C for 60 min, performed under flowing oxygen. Quantitative phase analysis using the Rietveld method reveals the identities and phase fractions of intermediates of P3-Na_xMnO_2, P2′-Na_xMnO_2, YOCl, Y_3O_4Cl, Y_2O_3; products of NaCl and $Y_2Mn_2O_7$; and a small amount of Na_3MnO_4 impurity, as

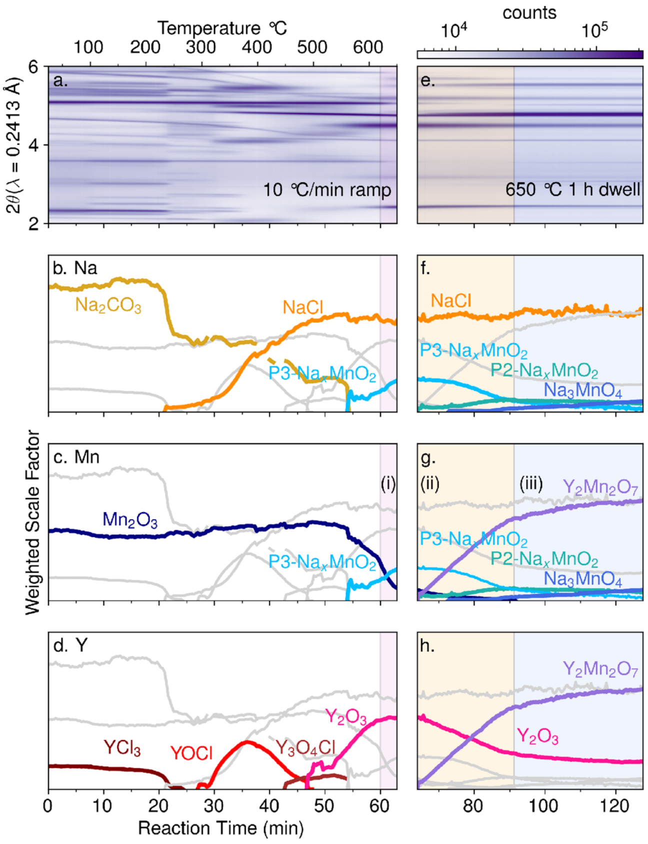

Figure 1. *In situ* SPXRD data and calculated weighted scale factors from sequential Rietveld analysis as a function of time for the reaction: $Mn_2O_3 + 2\ YCl_3 + 3\ Na_2CO_3 + 1/2\ O_2 \rightarrow Y_2Mn_2O_7 + 6\ NaCl + 3\ CO_2$ under flowing oxygen. The reaction is separated into two main vertical panels: (Panels a−d) heating at 10 °C/min to 650 °C and (panels e−h) dwelling at 650 °C for 60 min. (a,e) The *in situ* diffraction data plotted using a false color representation of the diffraction counts. Calculated weighted scale factors of phases over the course of the reaction are plotted and separated into horizontal panels by cation element: (b,f) sodium, (c,g) manganese, and (d,h) yttrium. The gray lines in each horizontal panel show the observed phases containing the other cations. The shaded regions, (i), (ii), and (iii), correspond to trajectories highlighted in Figure 5.

summarized in Figure 1. No other yttrium manganese oxide phases were observed.

The relevant intermediates that exist at the onset of formation of $Y_2Mn_2O_7$ are Y_2O_3, P3-Na_xMnO_2, and a small amount of Mn_2O_3. Y_2O_3 forms with a very small particle size (less than ∼35 nm, Figure S2), and its production yields a large fraction of the expected NaCl product (Figure 1). P3-Na_xMnO_2 forms directly from the reaction of Na_2CO_3 and Mn_2O_3, in agreement with a previous *in situ* and computational study.[9] Once both of these key intermediates are present, P3-Na_xMnO_2 then reacts with Y_2O_3 to form pyrochlore $Y_2Mn_2O_7$, also triggering the formation of P2′-Na_xMnO_2 (*Cmcm* structure, with a slight shear of the ideal P2-$P6_3/mmc$ structure).[35−37] Thereafter, selective formation of $Y_2Mn_2O_7$ is sustained through the reaction of P2′-Na_xMnO_2 with Y_2O_3. After P3-Na_xMnO_2 is fully consumed, the rate of $Y_2Mn_2O_7$ production slows dramatically, as Na_3MnO_4 gradually forms (Figure 1). Na_3MnO_4 does not appear in reaction products of *ex situ* studies of these assisted metathesis reactions performed on bulk scales, although it may be present as a trace quantity.[15]

Thermodynamic Stability of $Y_2Mn_2O_7$. Evaluation of the Y−Mn−O phase diagram reveals that $Y_2Mn_2O_7$ is thermodynamically stable (i.e., it is on the convex hull) at low temperatures (T ≤ 1100 °C). Using error-corrected formation energies derived from DFT calculations[38] and a previous Gibbs free energy model for solids,[28] the phase diagram of the Y−Mn−O system has been calculated at finite temperatures relevant to the synthesis reactions being investigated, with results of calculations at 650 and 1200 °C shown in Figure 2. Figure 2a depicts that the predominance area of $Y_2Mn_2O_7$ is quite small, indicating its low relative stability with respect to thermodynamic decomposition into neighboring phases. For a 1:1 Y:Mn composition ratio in an environment open to oxygen, h-$YMnO_3$ is thermodynamically stable at all temperatures and under a wide range of oxygen chemical potentials, while $Y_2Mn_2O_7$ is thermodynamically stable only below ∼1100 °C and at higher oxygen chemical potentials (i.e., oxygen rich conditions). The predicted temperature below which $Y_2Mn_2O_7$ is stable is overestimated by these calculations, since only h-$YMnO_3$ was observed to form at 950 °C in experiments.[17] Therefore, the low-temperature thermodynamic stability of $Y_2Mn_2O_7$ is assessed experimentally here by heating $Y_2Mn_2O_7$ in flowing oxygen at 650 °C for 2 weeks (Figure S12), a result that is in agreement with previous thermogravimetric analysis.[19] The fact that the Li_2CO_3 and K_2CO_3 precursors do not produce the thermodynamically favored phase of $Y_2Mn_2O_7$ at temperatures below 950 °C and $p(O_2) = 1$ atm (i.e., $\mu_O - \mu_O^0 \approx 0$) indicates that the metathesis reaction temperatures are sufficiently low to yield kinetic control in the formation of o-$YMnO_3$ or h-$YMnO_3$.[39] Finally, it indicates the need for a deeper understanding of the specific factors that determine which reaction pathway is followed for a given alkali carbonate precursor.

Product Selectivity via Chemical Potential Distances. We hypothesize that the generalized chemical potential diagram, which was previously devised as a three-dimensional extension of predominance diagrams with application to modeling interface stability and reactivity,[30] clarifies the large differences in product selectivity that arise by changing the identity of the alkali precursor. As the mathematical dual to the convex hull of the extensive energy-composition space, the generalized chemical potential diagram explicitly defines phase stability regions as bounded convex n−1-dimensional polytopes within the full n-dimensional, intensive chemical potential space. Although, in principle, the chemical potential diagram conveys identical information as the traditional compositional phase diagram, it has the unique advantage of directly revealing the *relative* stability of phases. In fact, the volume of each phase's stability polytope increases with its energy "below" the convex hull, i.e., the energy that would be released forming this phase via decomposition from the neighboring phases within a facet of the hull. The chemical potential diagram also directly links thermodynamic phase construction with atomic diffusion, and its construction even permits the visualization of diffusion paths in solid-state reactions.[30] Hence, the chemical potential diagram is well-suited for application to an understanding and prediction of the local behavior of reactions at solid interfaces.

Selective reactions in solid state chemistry need to minimize the probability of forming an undesired product phase at any point in time during the reaction pathway. As has been previously proposed,[40] a reaction at the interface between two solid phases can proceed through either interface control or

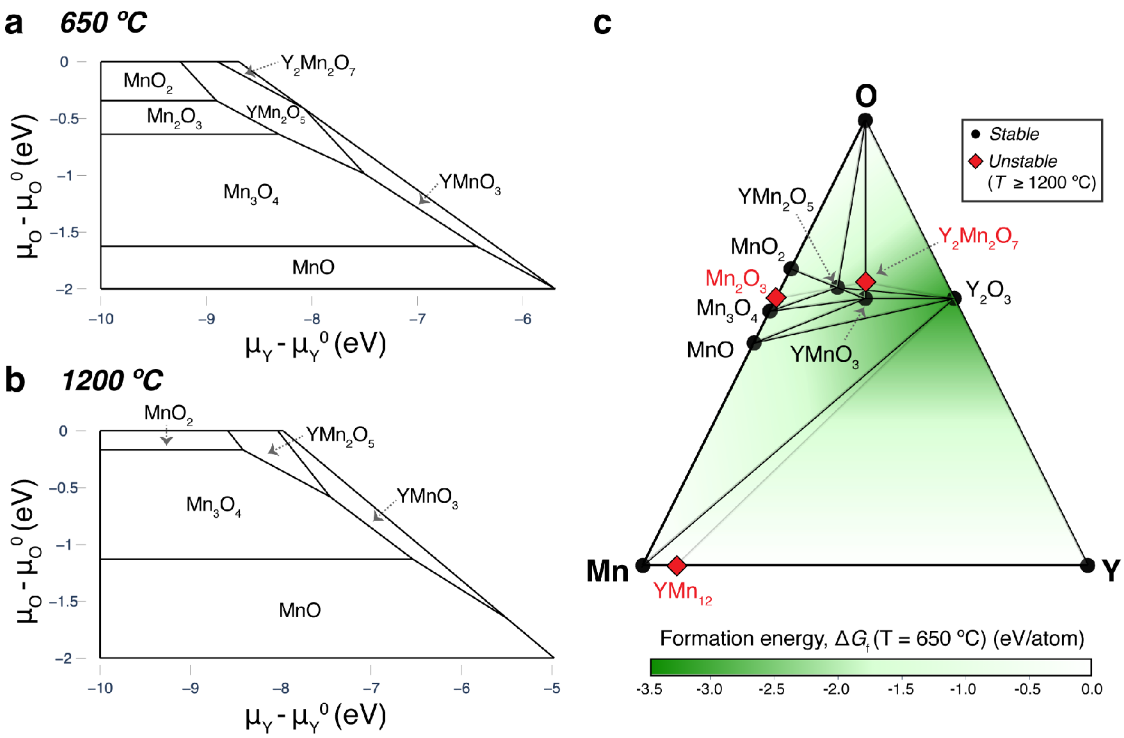

Figure 2. Computed phase stabilities in the Y−Mn−O chemical system. Predominance diagrams are shown as a function of oxygen and yttrium chemical potentials, μ_O and μ_Y, at temperatures of (a) 650 °C and (b) 1200 °C, referenced to their standard elemental state. (c) Predicted ternary compositional phase diagram for the Y−Mn−O system at 1200 °C (black lines/circles) overlaid on the phase diagram at 650 °C, where red squares and gray lines mark phases and facets that are destabilized at T ≥ 1200 °C, respectively. $Y_2Mn_2O_7$ is predicted to be stable at low temperatures ($T \leq 1100$ °C). Gibbs free energies of formation are estimated by applying a machine-learned transformation[28] on DFT-based formation enthalpies acquired from the Materials Project database.[27]

diffusion control, the latter resulting in local thermodynamic equilibrium and the corresponding requirement that elemental chemical potentials be continuous across the interfaces between reactants and product phase(s). All solid-state reactions eventually tend toward diffusion control as the product layer thickness grows. For this reason, predicted reactions which pose synthetic challenges are those in which it is impossible to achieve local equilibrium without decomposition to other phases before formation of the equilibrium product. On the chemical potential diagram, such reactions involve reactant-product pairs which do not share a phase boundary. Considering the reaction $Y_2O_3 + Mn_2O_3 \rightarrow 2\ YMnO_3$, if local equilibrium is achieved during the reaction, then according to Figure 3a, one expects YMn_2O_5 and/or Mn_3O_4 to form before formation of the final $YMnO_3$ product, consistent with the results of control reactions presented in Figure S10 and the previously reported phase diagram.[17]

Therefore, selective reactions are those which can be balanced, produce the desired product, and minimize the distance in chemical potential space between pairwise reactant-product interfaces. On the chemical potential diagram, this manifests as determination of whether each reactant-product pair shares a boundary (i.e., zero distance) or is separated by the polytope(s) of one or more additional phases (i.e., nonzero distance). This also applies to product−product pairs, which may further react if they do not share a boundary on the chemical potential diagram. Plotting of trial reactants in the three-dimensional chemical potential subspace of the product (Figure 3a) or the plotting of products in the reactant subspace (Figure 3b-d) permits direct visualization of the pairwise interfaces that control reactivity.[8,9] This “chemical potential distance”, $\Delta\mu_{\min}$ is geometrically calculated for all reactant-product and product−product interfaces in a reaction by determination of the minimum Euclidean distance between polytopes (see Methods). The primary advantage of calculating a distance value rather than a Boolean variable for whether or not two phases share a boundary is that the distance is more robust against inaccuracies in thermochemical data and conveys the degree to which the competing phases may interfere with the selectivity of the reaction.

Visualization of three-dimensional slices of the full Y−Mn−O−Na−Li−K chemical potential space reveals why only the sodium-based intermediates lead to formation of $Y_2Mn_2O_7$. Figure 3a illustrates slices of the stoichiometric $AMnO_2$ intermediates in the Y−Mn−O product chemical potential space. The $NaMnO_2$ stability polyhedron extends well beyond the range of both the $LiMnO_2$ and $KMnO_2$ phases. In fact, this Na-containing phase extends into high enough μ_O values to reach the stability area for $Y_2Mn_2O_7$. This enhanced stability of the $NaMnO_2$ phase into higher oxygen (and lower manganese) chemical potentials suggests that it may be uniquely capable of forming a stable interface with $Y_2Mn_2O_7$ and facilitating direct reaction to this pyrochlore phase. Specifically, the nearly shared boundary between the $NaMnO_2$ intermediate and $Y_2Mn_2O_7$ means that the reaction kinetics should be facile since the local chemical potentials of Mn and O do not need to change as the intermediate converts to the product. Furthermore, even though the *global* oxygen chemical potential is controlled through partial pressure of O_2, the reaction of $NaMnO_2$ provides *locally* available oxygen at the chemical potential required to form $Y_2Mn_2O_7$. In the case of the A = Li, K precursors, the lack of available oxygen with an appropriately

https://doi.org/10.1021/jacs.1c06229
J. Am. Chem. Soc. XXXX, XXX, XXX−XXX

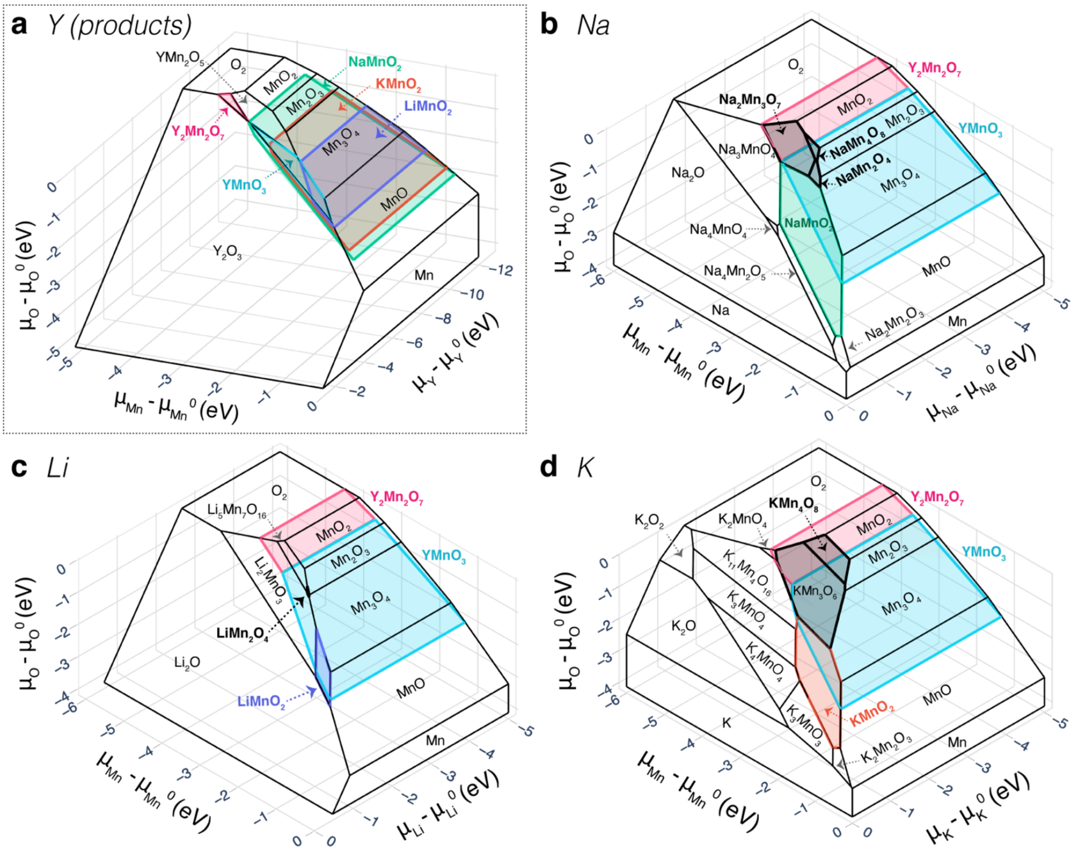

Figure 3. Chemical potential diagrams of the Y−Mn−O−Na−Li−K system at 650 °C, plotted in product (boxed) and reactant subspaces. (a) Y−Mn−O product subspace where the stability polytopes of stoichiometric $NaMnO_2$ (green), $LiMnO_2$ (purple), and $KMnO_2$ (orange) have been plotted as lower-dimensional slices, appearing as thin polyhedra due to the added degree of freedom (μ_Y). The $NaMnO_2$ polyhedron extends to high enough μ_O and low enough μ_{Mn} to reach $Y_2Mn_2O_7$, while the $LiMnO_2$ and $KMnO_2$ polyhedra do not. As such, $LiMnO_2$ and $KMnO_2$ suggest the formation of $YMnO_3$ and/or YMn_2O_5 depending on the value of μ_Y, as previously observed.[15,21,22] (b−d) A−Mn−O reactant subspaces with visualized slices of the $YMnO_3$ (cyan) and $Y_2Mn_2O_7$ (magenta) polytopes. The other shaded areas (gray) highlight A_xMnO_2 intermediates (and structurally related neighbors) that lead directly to the formation of yttrium manganese oxide products.

high chemical potential necessitates the reaction to proceed through other intermediates before it is even possible to reach $Y_2Mn_2O_7$.

The complementary inverse slices of the Y−Mn−O ternaries within the reactant A−Mn−O spaces (Figure 3b−d), along with the study of the atomic structures of the $AMnO_2$ phases, provide further explanation as to why the sodium-based intermediates facilitate reaction to $Y_2Mn_2O_7$ even for Na-deficient phases, Na_xMnO_2 (where $x < 1$). In agreement with prior work,[41] the sodium-based phases show a strong preference for the layered α-$NaFeO_2$-type structures relative to tunnel-like (e.g., Ramsdellite-derived) or spinel-derived structures. $Na_2Mn_3O_7$, $NaMn_2O_4$, and $NaMn_4O_8$, illustrated as gray shaded areas in Figure 3b, are all predicted to share the structurally analogous layered framework with stoichiometric $NaMnO_2$ (Figure S15a). Together, these structures create an interconnected pathway along the Na−Mn−O chemical potential surface toward higher oxygen chemical potentials where the surface touches the $Y_2Mn_2O_7$ product (e.g., oxidation states ranging from +3 to +5 depending on the nature of the vacancies and whether the composition is Na-poor or Mn-poor). In contrast, $LiMnO_2$ has a narrower range of stability than its neighboring Li−Mn−O phases, which each prefer distinct nonlayered structures (Figure S15b). In both the Li_2CO_3 assisted metathesis reactions[21] and the direct reaction between $LiMnO_2$ and YOCl,[22] we observed formation of $YMnO_3$ and YMn_2O_5, suggesting that the decreased range of chemical potentials over which layered $LiMnO_2$ is stable, and lack of structural homology between the Li_xMnO_2 phases inhibits the accessibility of $Y_2Mn_2O_7$ (e.g., due to rearrangement of the phases into spinel-derived structures). Finally, in the K_2CO_3 assisted metathesis reactions, no product selectivity was observed as the reaction produced a mixture of $YMnO_3$, YMn_2O_5, and $Y_2Mn_2O_7$ products.[21] While the K_xMnO_2 phases indeed exhibit a similar extension into high oxygen chemical potentials akin to Na_xMnO_2 (Figure 3d), the stoichiometric $KMnO_2$ ground-state structure does not follow the layered (nor even another another common) MnO_2 framework,[41] (Figure S15c) although the layered phase is predicted to be about 44 meV/atom higher in energy than the ground state. We thus conclude that similar to Li, the K-based system lacks the structural connectivity for interconversion between different K_xMnO_2 intermediates, although direct formation of K-deficient phases may promote formation of $Y_2Mn_2O_7$. In both the Li and K systems, the initial formation of $YMnO_3$ or YMn_2O_5 hence imposes significant kinetic barriers to the formation of $Y_2Mn_2O_7$. According to the chemical potential diagrams, $YMnO_3$ would have to decompose into YMn_2O_5 and Y_2O_3 en route to forming $Y_2Mn_2O_7$, which is consistent with myriad control experiments between binary yttrium and manganese oxides, with or without the presence of sodium (see Figures S10 and S11). Based on these observations, we

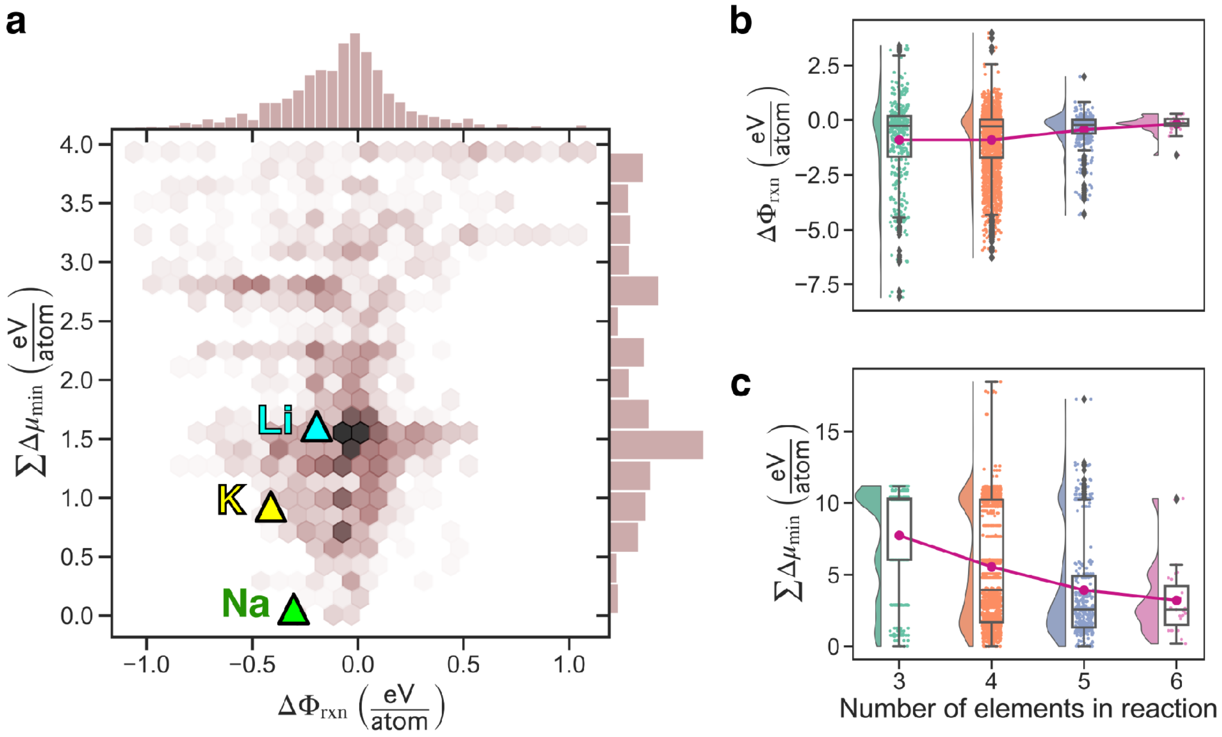

Figure 4. Energy and total chemical potential distance distributions for 3017 predicted chemical reactions forming $Y_2Mn_2O_7$. The reactions were predicted from a chemical space consisting of all alkali metals (Li, Na, K, Rb, Cs), halogens (F, Cl, Br, I), carbon (C), and the target elements (Y, Mn, O). Oxygen was treated as an open element with a chemical potential corresponding to μ_O^0 (p = 0.1 MPa, T = 650 °C). (a) A hexbin plot showing the distribution of reaction energies (in grand potential), $\Delta\Phi_{rxn}$, and calculated total chemical potential distance values, $\sum\Delta\mu_{min}$) for each reaction. The three colored triangles indicate the specific reactions 2 AMnO$_2$ + 2 YOCl + 1/2 O_2 → $Y_2Mn_2O_7$ + 2 ACl for A=Li, Na, K. (b,c) Distributions of reaction energies and total chemical potential distances as a function of the number of elements in the reaction. All reactions include at least the three elements of the target phase (Y, Mn, O). The mean values for each distribution are connected by a magenta line.

argue that the minimized chemical potential distance presented in Figures 3 and 4 and ability of sodium-based intermediate to interconvert across a wide range of stoichiometries and oxidation states explain why sodium provides selectivity of $Y_2Mn_2O_7$ via a kinetically viable pathway at lower temperatures.

Analysis of 3017 unique chemical reactions predicted to form $Y_2Mn_2O_7$ within the full alkali metal (Li, Na, K, Rb, Cs), halogen (F, Cl, Br, I), carbon (C), and target (Y, Mn, O) chemical system show that the Na-based ternary metathesis reaction, 2 $NaMnO_2$ + 2 YOCl + 1/2 O_2 → $Y_2Mn_2O_7$ + 2 NaCl is the most optimal reaction for both minimizing the total chemical potential distance and maximizing the (negative) grand potential energy of reaction, $\Delta\Phi_{rxn}$, when these two parameters are weighted equally (see Methods). This result suggests that the Na-based pathway is not only a good pathway for producing $Y_2Mn_2O_7$ but also may be the most suitable metathesis reaction for making this product. The full set of reactions and their weighted rankings can be found in provided data in the Supporting Information. The energy and total chemical potential distributions for these reactions illustrate that the Na-based reaction (green triangle in Figure 4a) optimizes both total chemical potential distance and overall reaction energy. The Na-based reaction has a near-zero total chemical potential distance (0.055 eV/atom) that is significantly smaller than those of the Li and K reactions (1.608 and 0.924 eV/atom respectively) and has a more negative reaction energy than any other reaction pathway with a near-zero total chemical potential distance. Figure 4 also reveals a major design principle behind using an expanded chemical space with metathesis reactions—the addition of other elements beyond those of the target phase (Y, Mn, O) can decrease the mean total chemical potential distance of the reaction without significantly changing the mean reaction energy. This hence provides many more opportunities for finding selective reactions beyond those that exclusively contain the target chemical species, i.e., 3,017 reactions in the full 13-element chemical system vs 362 potential reactions in the Y−Mn−O chemical system.

Direct ternary metathesis reactions carried out between Na_xMnO_2 and YOCl do indeed form $Y_2Mn_2O_7$ as predicted, but they also reveal important mechanistic details missing from the presented thermodynamic analysis that impact product selectivity. For example, available density functional theory data is highly focused on stoichiometric compounds but tends to be lacking for solid solution and defect-containing phases. Reaction of $NaMnO_2$ + YOCl in flowing O_2(g) results in some $Y_2Mn_2O_7$ formation but also the formation of $YMnO_3$ and YMn_2O_5 (Figure S13), suggesting that the evolution of the Na_xMnO_2 precursor during the reaction is important to consider, as illustrated in Figure 3b. A partially oxidized precursor in the reaction P2′-$Na_{0.7}MnO_2$ + YOCl selectively yields $Y_2Mn_2O_7$, but the reaction is incomplete after 24 h (Figure S14). Together, these control reactions suggest that the reaction rates also depend on the specific nature of defects present in the reactants and intermediates.

Mechanistic Facilitation through Defect Reactions. As the reaction pathway of the Li-based assisted metathesis reaction was previously reported,[21] we focus on how Na_xMnO_2-based intermediates react in a manner consistent

https://doi.org/10.1021/jacs.1c06229

with the predicted thermodynamic connectivity. Crystallographic analysis of the Na_xMnO_2 phases by free refinement of the crystallographic site occupancies of all elements in each Na_xMnO_2 structure and their subsequent analysis on an f^* diagram[25] reveal how the stoichiometry of Na_xMnO_2 changes through three different defect reactions along the reaction pathway for P3-Na_xMnO_2 (Figure 5) and for P2′-Na_xMnO_2 (Figure S7). While the exact compositions defined by the site occupancies are correlated with other refinement variables (e.g., atomic displacement parameters, as addressed in the SI), the compositional trajectories observed in Figure 5 are robust.[25] Two distinct compositional trajectories of the P3-Na_xMnO_2 phase on Figure 5 follow two major processes during the reaction pathway: (i) P3-Na_xMnO_2 formation and (ii) reaction of P3-Na_xMnO_2 to yield $Y_2Mn_2O_7$ and P2′-Na_xMnO_2. Additionally, delineation of trajectory (iii) describes when P2′-Na_xMnO_2 begins reacting to yield $Y_2Mn_2O_7$.

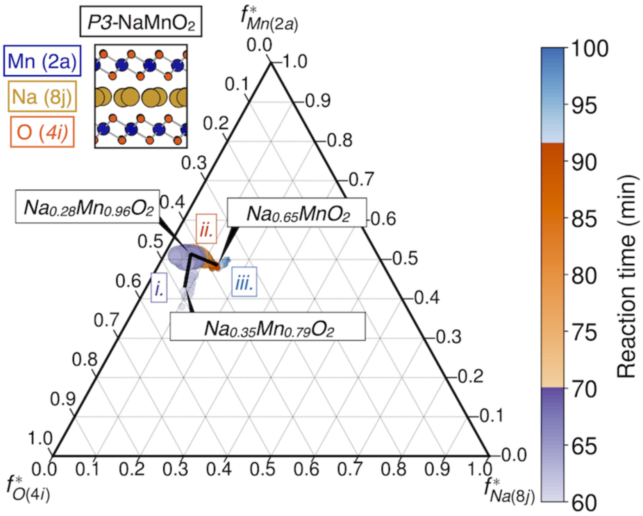

Figure 5. Compositional variation of the P3-Na_xMnO_2 intermediate determined by Rietveld analysis. In the f^* diagram, each axis denotes the X-ray scattering power from a crystallographic Wyckoff site within the lattice. For reference, calculated trajectories that correspond to the different stoichiometries of P3-Na_xMnO_2 are provided as black lines. The color bar in the figure follows the evolution of the P3-Na_xMnO_2 intermediate in the assisted metathesis reaction presented in Figure 1 with highlighted trajectories (i−iii) reflecting shaded regions in Figure 1(i−iii). The diameter of each circle mirrors the calculated weighted scale factor (WSF) in Figure 1 for P3-Na_xMnO_2 and thus corresponds to the amount of this layered phase. The structure of P3-Na_xMnO_2 is shown with Wyckoff atom sites labeled. The figure contains compositions for which the WSF is greater than 20% of the maximum WSF for the phase shown in Figure 1. Detailed analysis of individual site occupancies is provided in the SI.

The reaction of the P3-Na_xMnO_2 follows a compositional trend in chemical potential space toward the $Y_2Mn_2O_7$ product (Figure 3). The initial formation of P3-Na_xMnO_2 results in a very sodium-deficient composition, P3-$Na_{0.29}Mn_{0.96}O_2$. This manifests crystallographically as an excess of scattering intensity on the sodium site relative to the manganese site, suggestive of antisite disorder, as well as decreased scattering relative to oxygen, suggestive of metal deficiency (Figure 5, as described in detail in the SI), which is also observed in the initial formation of $LiNiO_2$.[42] Additionally, there is decreased scattering intensity of the metal sites relative to oxygen, which suggests the existence of overall cation deficiencies in the structure, calculated as $Na_{0.35}Mn_{0.79}O_2$ from Rietveld analysis of the PXRD data. The composition evolves in time through a cation-ordering reaction, where manganese occupying the (8*j*) sodium site moves to the manganese (2*a*) site (trajectory (i) in Figure 5). Movement along trajectory (i) yields site ordering as the phase fraction increases; the proposed stoichiometry is analytically calculated as the black line overlaid on these data in Figure 5 (see eqs S3 and S4). This ordering reaction yields a calculated composition of P3-$Na_{0.29}Mn_{0.96}O_2$ at its maximal phase fraction observed in Figure 1. At that point in the overall reaction, this intermediate with a relatively high oxygen chemical potential (Figure 3b) reacts to form $Y_2Mn_2O_7$.

There is a change in the defect chemistry of P3-Na_xMnO_2 consistent with the loss of Mn^{4+} + 2 O^{2-}, concomitant with consumption of Y_2O_3 and production of $Y_2Mn_2O_7$ and P2′-Na_xMnO_2. Along trajectory (ii) in Figure 5, there is a decrease in relative electron density from the oxygen site (4*i*) as well as an increase in the sodium to manganese site ratio, as described by eq 4. This reflects a change in defect chemistry along trajectory (ii) from the P3-$Na_{0.29}Mn_{0.96}O_2$ calculated composition at the end of trajectory (i) to that of P3-$Na_{0.65}MnO_2$. During this process, the pyrochlore phase fraction grows rapidly and P2′-Na_xMnO_2 is formed (Figure 1, at t = 70−90 min) before tapering off at the end of the second trajectory in Figure 5 as the amount of P3-Na_xMnO_2 is depleted.

Analysis of the *in situ* diffraction data reveals that selective formation of $Y_2Mn_2O_7$ occurs through two parallel reactions that start during trajectory (ii) in Figure 5

$$4\ \text{P3-}Na_{0.25}MnO_2 + Y_2O_3 \rightarrow 2\ \text{P2}'\text{-}Na_{0.5}MnO_2 + Y_2Mn_2O_7 \qquad (5a)$$

$$12\ \text{P2}'\text{-}Na_{0.5}MnO_2 + 8\ O_2 + 5\ Y_2O_3 \rightarrow 5\ Y_2Mn_2O_7 + 3\ Na_3MnO_4 \qquad (5b)$$

consistent with the predicted thermodynamic connectivity in Figure 3. In contrast, Li-based assisted metathesis reactions performed at temperatures between 500 and 850 °C proceed via $LiMnO_2$-based intermediates that result in the direct formation of $YMnO_3$ phase,[21,22] which is also predicted from the thermodynamic connectivity (Figure 3a,c).

On the basis of the stoichiometry of the residual Na−Mn−O phases in each step, there is a loss of Mn^{4+} + 2 O^{2-} along with the consumption of Y_2O_3. Thermodynamically, we expect that stoichiometric $NaMnO_2$ reacts with Y_2O_3 at a relatively high μ_O and low μ_{Mn} (see Figure 3b), as suggested by the average stoichiometry of the transferred species in the parallel cascade of defect reactions (eqs 5a and 5b). Curiously, the $Y_2Mn_2O_7$-forming reaction does not proceed via a typically labile topochemical deintercalation of the alkali cation[43] or oxygen anion,[3,4,44] but instead the chemical potential boundaries shown in Figure 3 guide the reaction to direct formation of the $Y_2Mn_2O_7$ product from the Na−Mn−O intermediates by avoiding the formation of other Y−Mn−O phases.

■ CONCLUSIONS

In assisted metathesis reactions, the presence of an appropriate alkali ion controls the selectivity of the reaction via differences in the thermodynamic stabilities of the reaction intermediates, as defined by the chemical potentials of the constituents in a hyperdimensional compositional space. In the reaction of 3 Na_2CO_3 + 2 YCl_3 + Mn_2O_3, the $Y_2Mn_2O_7$ pyrochlore is formed selectively via the direct reaction of Na_xMnO_2 and Y_2O_3 intermediates, as revealed by *in situ* temperature- and time-dependent SPXRD experiments. However, this pyrochlore selectivity is not achieved with the analogous Li_2CO_3 or K_2CO_3 precursors. Mapping the reaction species in chemical potential space illustrates that $NaMnO_2$, and structurally related compositional variants permit a small difference in local chemical potentials between the $Na_xMn_yO_2$ intermediates and $Y_2Mn_2O_7$, as the chemical stability windows of structurally homologous $Na_xMn_yO_2$ phases connect directly with that of $Y_2Mn_2O_7$. The short distance in chemical potential space illustrates why the reaction to form $Y_2Mn_2O_7$ is selective. In contrast, the other alkali-based (Li, K) intermediate phases lack the same degree of structural homology and share different boundaries, thus resulting in the formation of different products. The mechanistic details obtained from crystallographic analysis highlight that the thermodynamic boundaries dictate the reactivity rather than the mobility of an alkali cation within the oxide framework. This analysis illustrates how local thermodynamic equilibrium principles provide a direct connection to reaction kinetics in guiding the mechanistic pathway of solid-state reactions, thus providing a notion of a protecting group in materials synthesis. The thermodynamic underpinnings permit high-throughput prediction of precursors in higher dimensional chemical spaces that can impart selectivity, kinetic viability, and reversibility.

■ ASSOCIATED CONTENT

Supporting Information

The Supporting Information is available free of charge at https://pubs.acs.org/doi/10.1021/jacs.1c06229.

> Assisted metathesis reaction energetics, detailed description of the Na-based reaction progression, testing of alternative $NaMnO_2$ polytypes, *ex situ* control experiments, comparison of neighboring ternary oxide structures in chemical potential space, and Pareto frontier of predicted reactions forming $Y_2Mn_2O_7$ (PDF)
>
> Full set of enumerated chemical reactions, experimental raw data, processed data, data processing scripts, and figure plotting scripts (ZIP)

■ AUTHOR INFORMATION

Corresponding Author

James R. Neilson − *Department of Chemistry, Colorado State University, Fort Collins, Colorado 80523-1872, United States;* orcid.org/0000-0001-9282-5752; Email: james.neilson@colostate.edu

Authors

Paul K. Todd − *Department of Chemistry, Colorado State University, Fort Collins, Colorado 80523-1872, United States;* orcid.org/0000-0001-5409-3634

Matthew J. McDermott − *Materials Sciences Division, Lawrence Berkeley National Laboratory, Berkeley, California 94720, United States; Department of Materials Science and Engineering, University of California, Berkeley, California 94720, United States;* orcid.org/0000-0002-4071-3000

Christopher L. Rom − *Department of Chemistry, Colorado State University, Fort Collins, Colorado 80523-1872, United States;* orcid.org/0000-0002-6176-3197

Adam A. Corrao − *Department of Chemistry, Stony Brook University, Stony Brook, New York 11794-3400, United States;* orcid.org/0000-0001-6111-8959

Jonathan J. Denney − *Department of Chemistry, Stony Brook University, Stony Brook, New York 11794-3400, United States;* orcid.org/0000-0002-7615-997X

Shyam S. Dwaraknath − *Materials Sciences Division, Lawrence Berkeley National Laboratory, Berkeley, California 94720, United States;* orcid.org/0000-0003-0289-2607

Peter G. Khalifah − *Department of Chemistry, Stony Brook University, Stony Brook, New York 11794-3400, United States; Department of Chemistry, Brookhaven National Laboratory, Upton, New York 11973, United States;* orcid.org/0000-0002-2216-0377

Kristin A. Persson − *Molecular Foundry, Lawrence Berkeley National Laboratory, Berkeley, California 94720, United States; Department of Materials Science and Engineering, University of California, Berkeley, California 94720, United States;* orcid.org/0000-0003-2495-5509

Complete contact information is available at: https://pubs.acs.org/10.1021/jacs.1c06229

Author Contributions

$These authors contributed equally to this work.

Notes

The authors declare no competing financial interest.

■ ACKNOWLEDGMENTS

This work was supported as part of GENESIS: A Next Generation Synthesis Center, an Energy Frontier Research Center funded by the U.S. Department of Energy, Office of Science, Basic Energy Sciences under Award Number DE-SC0019212. We would also like to acknowledge the facilities at 17-BM-B at the Advanced Photon Source at Argonne National Laboratory and, in particular, the support of A. Yakovenko, W. Xu. JRN acknowledges partial support from a Sloan Research Fellowship. Theoretical calculations completed in this research used resources of the National Energy Research Scientific Computing Center (NERSC), a U.S. Department of Energy Office of Science User Facility operated under Contract No. DE-AC02-05CH11231.

■ REFERENCES

(1) Stein, A.; Keller, S. W.; Mallouk, T. E. Turning Down the Heat: Design and Mechanism in Solid-State Synthesis. *Science* **1993**, *259*, 1558−1564.

(2) Murphy, D. W.; Cros, C.; di Salvo, F. J.; Waszczak, J. V. Preparation and properties of Li_xVS_2 ($0 \leqslant x \leqslant 1$). *Inorg. Chem.* **1977**, *16*, 3027−3031.

(3) Tsujimoto, Y.; Tassel, C.; Hayashi, N.; Watanabe, T.; Kageyama, H.; Yoshimura, K.; Takano, M.; Ceretti, M.; Ritter, C.; Paulus, W. Infinite-layer iron oxide with a square-planar coordination. *Nature* **2007**, *450*, 1062−1065.

(4) Yajima, T.; Takeiri, F.; Aidzu, K.; Akamatsu, H.; Fujita, K.; Yoshimune, W.; Ohkura, M.; Lei, S.; Gopalan, V.; Tanaka, K.; Brown, C. M.; Green, M. A.; Yamamoto, T.; Kobayashi, Y.; Kageyama, H. A labile hydride strategy for the synthesis of heavily nitridized $BaTiO_3$. *Nat. Chem.* **2015**, *7*, 1017−1023.

(5) Armand, M.; Tarascon, J. M. Building better batteries. *Nature* **2008**, *451*, 652−657.

(6) Havelia, S.; Wang, S.; Balasubramaniam, K. R.; Schultz, A. M.; Rohrer, G. S.; Salvador, P. A. Combinatorial substrate epitaxy: a new approach to growth of complex metastable compounds. *CrystEngComm* **2013**, *15*, 5434−5441.

(7) Ding, H.; Dwaraknath, S. S.; Garten, L.; Ndione, P.; Ginley, D.; Persson, K. A. Computational Approach for Epitaxial Polymorph

Stabilization through Substrate Selection. *ACS Appl. Mater. Interfaces* **2016**, *8*, 13086−13093.

(8) Miura, A.; Bartel, C. J.; Goto, Y.; Mizuguchi, Y.; Moriyoshi, C.; Kuroiwa, Y.; Wang, Y.; Yaguchi, T.; Shirai, M.; Nagao, M.; Rosero-Navarro, N. C.; Tadanaga, K.; Ceder, G.; Sun, W. Observing and Modeling the Sequential Pairwise Reactions that Drive Solid-State Ceramic Synthesis. *Adv. Mater.* **2021**, *33*, 2100312.

(9) Bianchini, M.; Wang, J.; Clément, R. J.; Ouyang, B.; Xiao, P.; Kitchaev, D.; Shi, T.; Zhang, Y.; Wang, Y.; Kim, H.; Zhang, M.; Bai, J.; Wang, F.; Sun, W.; Ceder, G. The interplay between thermodynamics and kinetics in the solid-state synthesis of layered oxides. *Nat. Mater.* **2020**, *19*, 1088−1095.

(10) Bonneau, P. R.; Jarvis, R. F.; Kaner, R. B. Rapid solid-state synthesis of materials from molybdenum disulphide to refractories. *Nature* **1991**, *349*, 510−512.

(11) Wiley, J. B.; Kaner, R. B. Rapid solid-state precursor synthesis of materials. *Science* **1992**, *255*, 1093−1097.

(12) Miura, A.; Ito, H.; Bartel, C. J.; Sun, W.; Rosero-Navarro, N. C.; Tadanaga, K.; Nakata, H.; Maeda, K.; Ceder, G. Selective metathesis synthesis of $MgCr_2S_4$ by control of thermodynamic driving forces. *Mater. Horiz.* **2020**, *7*, 1310−1316.

(13) Wustrow, A.; Key, B.; Phillips, P. J.; Sa, N.; Lipton, A. S.; Klie, R. F.; Vaughey, J. T.; Poeppelmeier, K. R. Synthesis and Characterization of $MgCr_2S_4$ Thiospinel as a Potential Magnesium Cathode. *Inorg. Chem.* **2018**, *57*, 8634−8638.

(14) Seshadri, R.; Brock, S. L.; Ramirez, A.; Subramanian, M.; Thompson, M. E. Advances in the development and growth of functional materials: Toward the paradigm of materials by design. *MRS Bull.* **2012**, *37*, 682−690.

(15) Todd, P. K.; Neilson, J. R. Selective Formation of Yttrium Manganese Oxides through Kinetically Competent Assisted Metathesis Reactions. *J. Am. Chem. Soc.* **2019**, *141*, 1191−1195.

(16) Kamata, K.; Nakajima, T.; Nakamura, T. Thermogravimetric study of rare earth manganites $AMnO_3$ (A = Sm,Dy,Y,Er,Yb) at 1200°C. *Mater. Res. Bull.* **1979**, *14*, 1007−1012.

(17) Balakirev, V. F.; Golikov, Y. V. Heterogeneous Phase Equilibria in Rare Earth-Mn-O Systems in Air. *Inorg. Mater.* **2003**, *39*, S1−S10.

(18) Fujinaka, H.; Kinomura, N.; Koizumi, M.; Miyamoto, Y.; Kume, S. Syntheses and physical properties of pyrochlore-type $A_2B_2O_7$ (A = Tl,Y; B = Cr,Mn). *Mater. Res. Bull.* **1979**, *14*, 1133−1137.

(19) Subramanian, M.; Torardi, C.; Johnson, D.; Pannetier, J.; Sleight, A. Ferromagnetic $R_2Mn_2O_7$ pyrochlores (R = Dy, Lu, Y). *J. Solid State Chem.* **1988**, *72*, 24−30.

(20) Gardner, J. S.; Gingras, M. J. P.; Greedan, J. E. Magnetic pyrochlore oxides. *Rev. Mod. Phys.* **2010**, *82*, 53−107.

(21) Todd, P. K.; Smith, A. M. M.; Neilson, J. R. Yttrium Manganese Oxide Phase Stability and Selectivity Using Lithium Carbonate Assisted Metathesis Reactions. *Inorg. Chem.* **2019**, *58*, 15166−15174.

(22) Todd, P. K.; et al. Defect-Accommodating Intermediates Yield Selective Low-Temperature Synthesis of $YMnO_3$ Polymorphs. *Inorg. Chem.* **2020**, *59*, 13639−13650.

(23) Chupas, P. J.; Chapman, K. W.; Kurtz, C.; Hanson, J. C.; Lee, P. L.; Grey, C. P. A versatile sample-environment cell for non-ambient X-ray scattering experiments. *J. Appl. Crystallogr.* **2008**, *41*, 822−824.

(24) Jiang, Z.; Ramanathan, A.; Shoemaker, D. P. In situ identification of kinetic factors that expedite inorganic crystal formation and discovery. *J. Mater. Chem. C* **2017**, *5*, 5709−5717.

(25) Yin, L.; Mattei, G. S.; Li, Z.; Zheng, J.; Zhao, W.; Omenya, F.; Fang, C.; Li, W.; Li, J.; Xie, Q.; Zhang, J.-G.; Whittingham, M. S.; Meng, Y. S.; Manthiram, A.; Khalifah, P. G. Extending the limits of powder diffraction analysis: Diffraction parameter space, occupancy defects, and atomic form factors. *Rev. Sci. Instrum.* **2018**, *89*, 093002.

(26) Yin, L.; et al. Thermodynamics of Antisite Defects in Layered NMC Cathodes: Systematic Insights from High-Precision Powder Diffraction Analyses. *Chem. Mater.* **2020**, *32*, 1002−1010.

(27) Jain, A.; Ong, S. P.; Hautier, G.; Chen, W.; Richards, W. D.; Dacek, S.; Cholia, S.; Gunter, D.; Skinner, D.; Ceder, G.; Persson, K. A. Commentary: The Materials Project: A materials genome approach to accelerating materials innovation. *APL Mater.* **2013**, *1*, 011002.

(28) Bartel, C. J.; Millican, S. L.; Deml, A. M.; Rumptz, J. R.; Tumas, W.; Weimer, A. W.; Lany, S.; Stevanović, V.; Musgrave, C. B.; Holder, A. M. Physical descriptor for the Gibbs energy of inorganic crystalline solids and temperature-dependent materials chemistry. *Nat. Commun.* **2018**, *9*, 4168.

(29) Ong, S. P.; Jain, A.; Hautier, G.; Kang, B.; Ceder, G. Thermal stabilities of delithiated olivine MPO_4 (M = Fe, Mn) cathodes investigated using first principles calculations. *Electrochem. Commun.* **2010**, *12*, 427−430.

(30) Yokokawa, H. Generalized chemical potential diagram and its applications to chemical reactions at interfaces between dissimilar materials. *J. Phase Equilib.* **1999**, *20*, 258.

(31) Patel, A. M.; Nørskov, J. K.; Persson, K. A.; Montoya, J. H. Efficient Pourbaix diagrams of many-element compounds. *Phys. Chem. Chem. Phys.* **2019**, *21*, 25323−25327.

(32) Virtanen, P.; et al. SciPy 1.0: fundamental algorithms for scientific computing in Python. *Nat. Methods* **2020**, *17*, 261−272.

(33) McDermott, M. J.; Dwaraknath, S. S.; Persson, K. A. A graph-based network for predicting chemical reaction pathways in solid-state materials synthesis. *Nat. Commun.* **2021**, *12*, 3097.

(34) McDermott, M.; Dwaraknath, S. GENESIS-EFRC/reaction-network: v2.0.3. 2021; DOI: 10.5281/zenodo.5165276.

(35) Caballero, A.; Hernán, L.; Morales, J.; Sánchez, L.; Santos Peña, J.; Aranda, M. A. Synthesis and characterization of high-temperature hexagonal P2-$Na_{0.6}MnO_2$ and its electrochemical behaviour as cathode in sodium cells. *J. Mater. Chem.* **2002**, *12*, 1142−1147.

(36) Paulsen, J.; Dahn, J. Studies of the layered manganese bronzes, $Na_{2/3}[Mn_{1-x}M_x]O_2$ with M = Co, Ni, Li, and $Li_{2/3}[Mn_{1-x}M_x]O_2$ prepared by ion-exchange. *Solid State Ionics* **1999**, *126*, 3−24.

(37) Clément, R. J.; Bruce, P. G.; Grey, C. P. Review-Manganese-based P2-type transition metal oxides as sodium-ion battery cathode materials. *J. Electrochem. Soc.* **2015**, *162*, A2589−A2604.

(38) Jain, A.; Hautier, G.; Ping Ong, S.; Moore, C. J.; Fischer, C. C.; Persson, K. A.; Ceder, G. Formation enthalpies by mixing GGA and GGA + U calculations. *Phys. Rev. B: Condens. Matter Mater. Phys.* **2011**, *84*, 45115.

(39) Martinolich, A. J.; Higgins, R. F.; Shores, M. P.; Neilson, J. R. Lewis Base Mediated Polymorph Selectivity of Pyrite $CuSe_2$ through Atom Transfer in Solid-State Metathesis. *Chem. Mater.* **2016**, *28*, 1854−1860.

(40) Schmalzried, H. *Solid state reactions*; Verlag Chemie, 1981.

(41) Kitchaev, D. A.; Dacek, S. T.; Sun, W.; Ceder, G. Thermodynamics of Phase Selection in MnO_2 Framework Structures through Alkali Intercalation and Hydration. *J. Am. Chem. Soc.* **2017**, *139*, 2672−2681.

(42) Bai, J.; Sun, W.; Zhao, J.; Wang, D.; Xiao, P.; Ko, J. Y. P.; Huq, A.; Ceder, G.; Wang, F. Kinetic Pathways Templated by Low-Temperature Intermediates during Solid-State Synthesis of Layered Oxides. *Chem. Mater.* **2020**, *32*, 9906−9913. Publisher: American Chemical Society.

(43) Neilson, J. R.; McQueen, T. M. Bonding, Ion Mobility, and Rate-Limiting Steps in Deintercalation Reactions with $ThCr_2Si_2$-type KNi_2Se_2. *J. Am. Chem. Soc.* **2012**, *134*, 7750−7757.

(44) Hayward, M. A.; Green, M. A.; Rosseinsky, M. J.; Sloan, J. Sodium hydride as a powerful reducing agent for topotactic oxide deintercalation: Synthesis and characterization of the nickel(I) oxide $LaNiO_2$. *J. Am. Chem. Soc.* **1999**, *121*, 8843−8854.